IEEE Journal of Microwaves

Received 12 June 2022; accepted 1 August 2022. Date of publication 24 August 2022;
date of current version 7 October 2022.

Digital Object Identifier 10.1109/JMW.2022.3196454

System Performance of a 79 GHz High-Resolution 4D Imaging MIMO Radar With 1728 Virtual Channels

DOMINIK SCHWARZ (Graduate Student Member, IEEE), NICO RIESE, INES DORSCH (Graduate Student Member, IEEE), AND CHRISTIAN WALDSCHMIDT (Fellow, IEEE)

(Regular Paper)

Institute of Microwave Engineering, Ulm University, 89081 Ulm, Germany

CORRESPONDING AUTHOR: Dominik Schwarz (e-mail: dominik-1.schwarz@uni-ulm.de).

ABSTRACT Future driver assistance and autonomous driving systems require high-resolution 4D imaging radars that provide detailed and robust information about the vehicle's surroundings, even in poor weather or lighting conditions. In this work, a novel high-resolution radar system with 1728 virtual channels is presented, exceeding the state-of-the-art channel count for automotive radar sensors by a factor of 9. To realize the system, a new mixed feedthrough and distribution network topology is employed for the distribution of the ramp oscillator signal. A multilayer printed circuit board is designed and fabricated with all components assembled on the back side, while the radio frequency signal distribution is on a buried layer and only the antennas are on the front side. The array is optimized to enable both multipleinput multiple-output operation and transmit beamforming. A sparse array with both transmit and receive antennas close to the transceivers is realized to form a 2D array with a large unambiguous region of $130^\circ \times 75^\circ$ with a maximal sidelobe level of -15 dB. The array features a 3 dB beamwidth of $0.78^\circ \times 3.6^\circ$ in azimuth and elevation, respectively. Radar measurements in an anechoic chamber show that even the individual peaks of the absorber in the chamber can be detected and separated in the range-angle cut of the 4D radar image. The performance is validated by measurements of a parking lot, where cars, a pedestrian, a fence, and a street lamp can be detected, separated, and estimated correctly in size and position.

INDEX TERMS Advanced driver assistance systems (ADAS), automotive radar, chirp sequence modulation, direction-of-arrival (DoA) estimation, frequency modulated continuous wave (FMCW), imaging radar, local oscillator (LO) feedthrough, mm-wave, multiple-input multiple-output (MIMO), time delay correction.

I. INTRODUCTION

Radar sensors are used in various areas of application as they are able to provide accurate information on range, velocity, and the direction-of-arrival (DoA) of surrounding objects, even under harsh environmental conditions [1]–[5]. By distributing the antennas in two dimensions, DoA estimation in both azimuth and elevation is enabled, yielding a 4D imaging system [6], [7]. This information depth is required for the development of autonomous driving and future advanced driver assistance systems (ADAS) in the automotive 77 / 79 GHz band [8]–[10]. However, especially in 4D imaging, a large number of channels is required to obtain an accurate DoA estimation with low sidelobes. A widely used approach requiring a reduced number of physical hardware channels is the multiple-input multiple-output (MIMO) principle [11]–[13].

The trend towards an ever increasing number of virtual (Vx) channels N_{Vx} and 2D DoA estimation can be observed when comparing older systems [14] with a more current one [15] with 128 virtual channels, see the overview given in Table 1. To realize larger systems with typically 192 virtual channels [16], four monolithic microwave integrated circuits (MMICs) with three transmit (Tx) and four receive (Rx) channels [17] are combined. Based on this topology, different systems with the majority of the channels distributed in the azimuth (az.) plane are realized. This leads either to a wide

TABLE 1. Overview of State-of-the-Art Automotive Radar Systems

Source	N_{Vx}	B / GHz	LO[a]	$\Delta\alpha$ / °	$\Delta\varepsilon$ / °
[14, 2011]	8 or 16	2	D	6.4	–
[15, 2018]	128	2	D	2.2	13
[18, 2020]	192	5	D	1.7	14
[19, 2020]	192	3.5	D	2.5	2.5
[20, 2021]	192	0.75	–	<3	<3
[21, 2022]	3 × 64	1	D	1.6	1.8 – 2.8
[22, 2018]	64	3	–	2.1	4.4
[24, 2019]	4	8	F	26	–
[25, 2021]	48	0.5	F	3.8	13
This work	1728	5	F / D	0.78	3.6

[a]: The FMCW signal is distributed: (D) with a passive distribution network or (F) within a feedthrough topology.

beamwidth [18] or a large sparsity [19] in the elevation (el.) plane. A different concept is to split the available channels into a small unambiguous array and a large array with narrow beamwidths and to resolve the ambiguities of the latter in the post-processing [20]. In [21], the 192 channels of a system with similar MMICs are divided into three radar subsystems with different field of views (FoVs) to cover different use cases and to resolve the ambiguities of each individual array.

In all these systems, a computationally intensive post-processing is required to resolve ambiguities, which is error-prone under poor conditions such as low signal-to-noise ratio (SNR) or in complex multi-target cases. For unambiguous, yet very sparse arrays as in [22], a complex reconstruction as shown in [8] is required to reduce the sidelobe level (SLL) in the DoA estimation, having the same limitations as above. To reduce the sparsity and thus effort in the post-processing, a higher channel count is required. In [23], four coherent groups with individual signal syntheses are combined to realize a system with 256 virtual channels with a reduced complexity in the distribution of the frequency modulated continuous wave (FMCW) signal. To further reduce the effort in terms of design time and hardware complexity, a feedthrough topology can be used, as already shown for small 3D [24] and 4D [25] radar systems. So far, the time delays in the signal distribution were a limiting factor in the design of such systems.

In this contribution, a novel 4D radar imaging system is presented. To overcome the limitations of previous systems, a large 2D antenna array with only minor sparsity is realized. This results in narrow beamwidths in both the azimuth and elevation plane and a low SLL enabling a robust DoA estimation. Furthermore, the very high channel count of 1728 results in a high processing gain and thus a superior detection capability. A combined system topology is realized, employing both length matched distribution networks and feedthrough lines to reduce the hardware effort. Through this combination, multiple Tx channels from different MMICs can be used for coherent Tx beamforming, while the time delay among all channels is easily corrected in the range-Doppler spectrum [26].

This paper is organized as follows: In Section II, the system concept is introduced and analyzed. The realized sensor is presented in Section III. In Section IV, the performance of the system is verified and finally shown in a realistic automotive scenario in Section V.

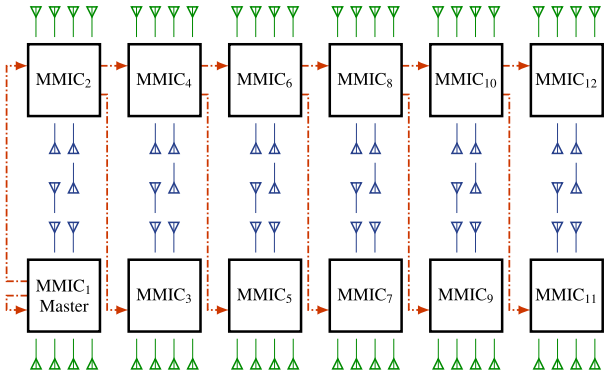

FIGURE 1. Schematic diagram of the high-resolution 4D imaging radar system. It is composed of 12 transceiver MMICs, each one incorporating 3 Tx (—) and 4 Rx (—) channels. Each 6 transmitters form a group, in which beamforming can be performed. The FMCW signal (- -) is distributed with a combination of passive distribution and a feedthrough topology.

II. SYSTEM CONCEPT

The proposed radar system as visualized by the system concept shown in Fig. 1 is composed of 12 transceiver MMICs resulting in a virtual array with 1728 channels. The MMICs are distributed in a 6 × 2 array to realize a very large aperture in azimuth and a large one in the elevation direction to meet the requirements of complex automotive radar scenarios. Each 6 Tx antennas are arranged as a 2 × 3 uniform rectangular array (URA) and thus form a group enabling Tx beamforming.

A. COMBINED FMCW SIGNAL DISTRIBUTION CONCEPT

The FMCW signal is generated in the ramp oscillator (RO) of one single MMIC at a quarter of the transmit frequency. This MMIC functions as master. Typically, two length matched 1-to-2 passive distribution networks are employed on the RO outputs of the master MMIC to feed all 4 MMICs of the 192 channel systems [16], [18]. In each MMIC, the RO signal is upconverted with a frequency multiplier [17], [27].

To enable Tx beamforming, both MMICs of one group require a phase synchronous RO signal. This can be achieved by using a length matched distribution network, which comes at the cost of a large space requirement on the PCB and the need of additional amplifiers when utilizing more than 4 MMICs. In the proposed system concept, each group is fed via length matched lines from one MMIC of the previous group, see (- →) in Fig. 1, realizing a mixed feedthrough and distribution topology. This way, only 12 length matched transmission lines and no amplifiers, power dividers, or large distribution networks are required. The lengths of the lines are chosen in such a way that they fulfill the power requirements of the RO inputs and allow an easy correction of the range offset as stated in the following.

In the general case, the length L_i of an individual transmission line in the distribution of the RO signal leads to a range

offset [26]

$$\Delta R = L_i \frac{\sqrt{\varepsilon_{\mathrm{r,eff}}}}{2}, \tag{1}$$

where $\varepsilon_{\mathrm{r,eff}}$ denotes the effective relative permittivity for the transmission line. Using the range resolution $\delta R = c_0/(2B)$ [4], the offset in range cells caused by the feedthrough topology is

$$\Delta i_{\mathrm{R,\,FTT}} = \frac{\Delta R}{\delta R} = L_i \frac{\sqrt{\varepsilon_{\mathrm{r,eff}}} \cdot B}{c_0}, \tag{2}$$

with the speed of light c_0 and the bandwidth B of the FMCW signal. This leads to a shift of the range cell $i_{\mathrm{R,\,Rx}}$ at which a peak is visible in the range spectrum. In the proposed topology with matched lengths L, $i_{\mathrm{R,\,Rx}}$ is given as

$$i_{\mathrm{R,\,Rx}} = \frac{R}{\delta R} + \Delta i_{\mathrm{R,\,FTT}} \left(I_{\mathrm{Group,\,Tx}} - I_{\mathrm{Group,\,Rx}}\right), \quad \text{with} \quad \left\{I_{\mathrm{Group}} \in \mathbb{N} | 1 \le I_{\mathrm{Group}} \le N_{\mathrm{Group}}\right\}, \tag{3}$$

where R denotes the actual range, I_{Group} the group index of the transmitting or receiving MMIC, and N_{Group} the number of MMIC groups. If the delay occurs in the feed of the receiving MMIC, the radar target appears to be closer; if it occurs in the feed of the transmitter, it appears to be farther away. By choosing the length L such that $\Delta i_{\mathrm{R,\,FTT}}$ is an integer, the offset can easily be corrected by shifting the range spectra (obtained after the range-Doppler processing [28]) by the corresponding number of range bins [26]:

$$i_{\mathrm{R,\,corr}} = \left|i_{\mathrm{R,\,Rx}}\right| - \Delta i_{\mathrm{R,\,FTT}} \left(I_{\mathrm{Group,\,Tx}} - I_{\mathrm{Group,\,Rx}}\right), \tag{4}$$

where the subtrahend is the required range cell shift. This correction leads to errors if the target response is shifted to negative range cells, see (3) for $I_{\mathrm{Group,\,Tx}} < I_{\mathrm{Group,\,Rx}}$. Due to the image frequency problem in case of real sampling [29], the target responses are detected at positive range cells, as indicated by the magnitude operator $|.|$ in (4). Thus, the correction is performed in the wrong direction. As this occurs only for targets closer than the maximum range offset ($(N_{\mathrm{Group}} - 1)\ \Delta i_{\mathrm{R,\,FTT}}$), typically only the Tx to Rx leakage signal is affected.

B. PCB TECHNOLOGY

A printed circuit board (PCB) layer stack as shown in Fig. 2 is used for the design of the proposed system. To prevent unwanted radiation, all radio frequency (RF) signals are routed on a buried stripline and the MMICs are placed on the back side of the PCB. This allows efficient cooling with large heat spreaders without affecting the antenna characteristics. Therefore, the top layer of the PCB is reserved exclusively for the antennas and no components are mounted on it.

By using an low-loss vertical transition through FR4 [30], the PCB can be fabricated in a cost effective high-density interconnect process. The losses of 2 dB from the MMICs into the stripline are comparable to a conventional MMIC to microstrip line transition.

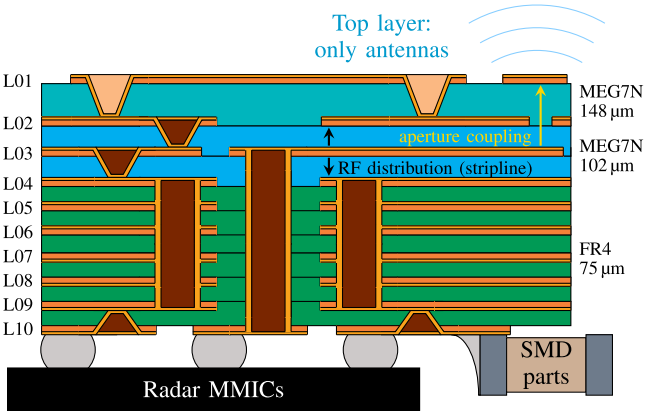

FIGURE 2. Sketch of the cross section of the multilayer PCB with antennas on top and the SMD assembly exclusively on the back side.

C. MIMO ANTENNA ARRAY

To reduce the RF line losses, the 3 Tx and 4 Rx antennas are located close to the individual MMICs. The antennas are placed on a grid with 2 mm spacing in azimuth, which is only slightly larger than the half-wavelength $\lambda/2$. In elevation, the grid is enlarged to 2.25 mm to increase the aperture size with a tolerable influence on the ambiguity-free region.

As each MMIC with its related surface mount device (SMD) parts occupies an area of about $30 \times 50\,\mathrm{mm}^2$, the Tx antenna groups are placed on a 30 mm grid, as shown in the optimized antenna array in Fig. 3. With the receivers located close to the MMICs, an interleaved sparse array with a hardware aperture size of $184 \times 40.5\,\mathrm{mm}^2$ is designed. Utilizing the genetic optimization from [6], the Rx antenna positions are optimized to adhere the design restrictions and to form an unambiguous array. The optimized Rx array performance is analyzed and shown in Fig. 4. An unambiguous Rx array enables an unambiguous 2D DoA estimation independent of number and positions of the transmitters. This is required for the arbitrary application of Tx beamforming. With the Rx array, i.e. the hardware aperture size, a narrow beam width of 0.9° in the azimuth and 4° in the elevation plane is realized, see Fig. 4(a). Since there is a gap between the Rx antennas in the middle of the aperture in the elevation direction, two main sidelobes with an SLL of -2.9 dB at $\pm 8^\circ$ disturb the angular spectrum. These are also clearly visible in the 2D angular spectrum of a target in broadside direction shown in (b). In (c), the the maximal SLL matrix $\mathbf{S}$ is shown on a logarithmic scale. Due to the two main sidelobes in elevation, the average maximal SLL is -2.9 dB. The receive array is unambiguous over a large angular area of $130^\circ \times 75^\circ$.

The maximal SLL matrix $\mathbf{S}$ is derived from the 4D ambiguity function of 2D antenna arrays to easily asses the ambiguity-free region and the SLL of 2D antenna arrays. The 4D ambiguity function is given as [31]

$$\chi\left(\alpha_i^r, \varepsilon_j^r, \alpha_k^e, \varepsilon_l^e\right) = \frac{\boldsymbol{v}^\dagger\left(\alpha_i^r, \varepsilon_j^r\right) \cdot \boldsymbol{v}\left(\alpha_k^e, \varepsilon_l^e\right)}{\left\|\boldsymbol{v}^\dagger\left(\alpha_i^r, \varepsilon_j^r\right)\right\| \left\|\boldsymbol{v}\left(\alpha_k^e, \varepsilon_l^e\right)\right\|}, \tag{5}$$

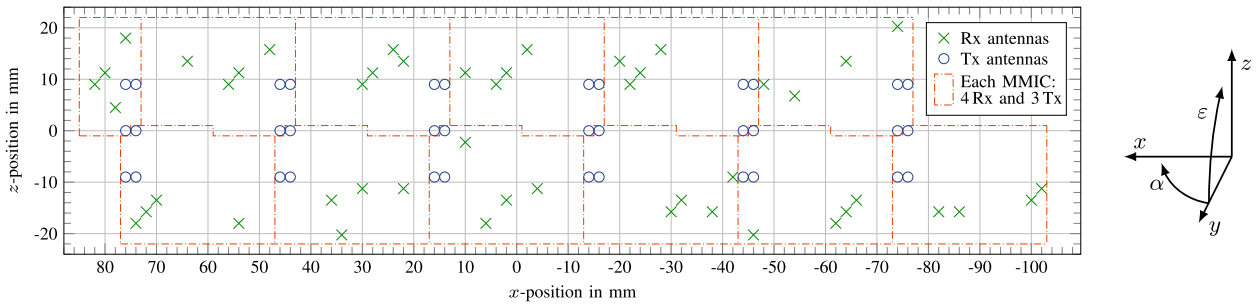

FIGURE 3. Diagram of the proposed and optimized antenna array with 48 Rx and 36 Tx channels from 12 radar transceivers.

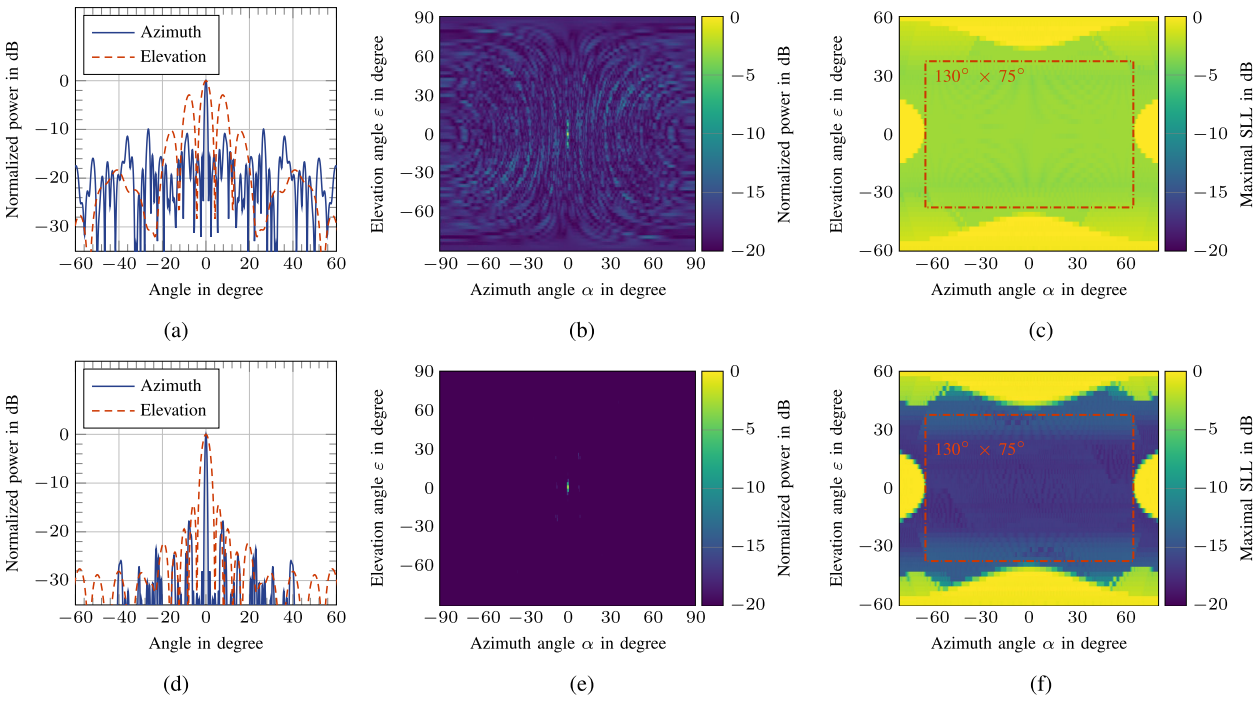

FIGURE 4. Evaluation of the optimized receive array ((a)–(c)) and the resulting virtual MIMO array ((d)–(f)): (a) and (d) show the azimuth and elevation beam pattern, (b) and (e) the 2D angle estimation for a target at broadside direction, and (c) and (f) the maximal SLL for all 2D angle estimations with the ambiguity-free region highlighted ( ).

with the 2D steering vector

$$\boldsymbol{v}(\alpha,\varepsilon) = \begin{pmatrix} \mathrm{e}^{-\mathrm{j}\frac{2\pi}{\lambda_0}(x_{\mathrm{Vx},1}\sin\alpha\cos\varepsilon + z_{\mathrm{Vx},1}\sin\varepsilon)} \\ \vdots \\ \mathrm{e}^{-\mathrm{j}\frac{2\pi}{\lambda_0}(x_{\mathrm{Vx},\mathrm{N_{Vx}}}\sin\alpha\cos\varepsilon + z_{\mathrm{Vx},\mathrm{N_{Vx}}}\sin\varepsilon)} \end{pmatrix}, \quad (6)$$

where x_{Vx} and z_{Vx} are the respective x- and z-positions of the virtual elements. The superscripts r and e indicate the real incident and estimated angle, λ_0 is the free-space wavelength at the start frequency of the FMCW ramp, and † and $\|.\|$ denote the transpose complex conjugate and the vector norm, respectively. It is calculated for the azimuth angles

$$\alpha_i = \alpha_0 + (i-1)\Delta\alpha \quad \text{or} \quad \alpha_k = \alpha_0 + (k-1)\Delta\alpha\,,$$

with the step size $\Delta\alpha$ and the integers i and k between 1 and the number of azimuth angles N, and the elevation angles

$$\varepsilon_j = \varepsilon_0 + (j-1)\Delta\varepsilon \quad \text{or} \quad \varepsilon_l = \varepsilon_0 + (l-1)\Delta\varepsilon\,,$$

with the step size $\Delta\varepsilon$ and the integers j and l between 1 and the number of elevation angles M. For a given incident angle pair α_i^r and ε_j^r, the matrix

$$\mathbf{X}_{ij}\left(\alpha_k^e, \varepsilon_l^e\right) = \chi\left(\alpha_i^r, \varepsilon_j^r\right), \text{ with } \mathbf{X}_{ij} \in [0,1]^{\mathrm{N}\times\mathrm{M}}, \quad (7)$$

represents an individual 2D angle estimation. Instead of determining the maximum sidelobe in each 2D angle estimation and classifying the corresponding incident angle as ambiguous or unambiguous (depending on the SLL maximum), the maximal SLL matrix is proposed here. By iterating through all incident angles in χ, first the main lobes are detected in each sub-matrix $\mathbf{X}_{ij}(\alpha_k^e, \varepsilon_l^e)$ and then set to zero:

$$\mathbf{X}_{ij}\left(\alpha_k^e, \varepsilon_l^e\right) = 0\,, \text{ if } \alpha_k^e, \varepsilon_l^e \text{ is part of the main lobe}\,. \quad (8)$$

TABLE 2. Overview of the Radar Operation Modes

Name	Tx elements az. × el.	Total gain / dB	3 dB width of AF[b] az. / °	el. / °
Standard MIMO	1 × 1	0	–	–
Az. BF	2 × 1	6	84	–
El. BF	1 × 2	6	–	10.6
Mid-range	1 × 3	10	–	6.9
Long-range	2 × 3	16	84	6.9

[b]: AF denotes the array factor for all radiating patches [32].

Next, all iterations are combined in the 4D sidelobe function $\chi_{\mathrm{SLL}}(\alpha_i^r, \varepsilon_j^r, \alpha_k^e, \varepsilon_l^e)$. Finally, the maximal SLL matrix

$$\mathbf{S}\left(\alpha_i^r, \varepsilon_j^r\right) = \max_{\alpha_k^e}\left(\max_{\varepsilon_l^e}\left(\chi_{\mathrm{SLL}}\left(\alpha_i^r, \varepsilon_j^r, \alpha_k^e, \varepsilon_l^e\right)\right)\right) \tag{9}$$

is obtained, which is shown in Fig. 4(c). Comparing **S** with a fixed threshold leads to the ambiguity indicator matrix **Q** as introduced in [6], but **S** gives a better visualization and insight on the array performance.

Taking also the Tx channels into account, a narrow 3 dB beamwidth of the virtual array of 0.78° in the azimuth plane and 3.6° in elevation is achieved, as shown in Fig. 4(d). In the virtual MIMO array, the gap in the elevation direction is filled, and the two main sidelobes from (a) vanish. The overall SLL is reduced to −15 dB and further decreases to the edges of the FoV. Thus, no major sidelobes disturb the whole 2D angular spectrum, see (e). As shown in Fig. 4(f), the virtual array has the same ambiguity-free region as the receive array but with a significantly lower maximal SLL resulting from the higher virtual channel count.

Spanning a virtual aperture of 85.2 λ_0 × 14.8 λ_0 with a URA of the same grid requires 4563 virtual channels. Hence, the 1728 available virtual channels correspond to a fill factor of 38 %, which is a high value for sparse 2D arrays, enabling a robust DoA estimation.

D. TX BEAMFORMING CAPABILITY

With the high number of virtual channels and the proposed system concept, Tx beamforming is enabled and at the same time the virtual array is still sufficient to perform 4D imaging. Therefore, the radar is designed to operate in five different operation modes as listed in Table 2. Using 2 × 2 Tx elements, a sixth mode enabling 2D beamforming is possible.

The 2 × 3 Tx URAs with an element spacing of Δx=2 mm and Δz=9 mm is conceptualized to operate with 1 (az.) × 4 (el.) patch antennas as individual elements. These achieve a moderate directivity while the full ambiguity-free region is illuminated. As no length matching is applied to the antenna feed lines to reduce the line losses, the phase difference between the individual transmit channels needs to be determined via a calibration measurement and compensated afterwards. The compensation can be performed by employing the integrated Tx phase shifters of the radar MMICs at no extra costs.

To maintain a high virtual channel count and thus enable 4D imaging, two elements are combined in azimuth or elevation for the beamforming (BF) operating modes. In order to steer the beam into a certain azimuth (α_{steer}) or elevation ($\varepsilon_{\mathrm{steer}}$) direction, the corresponding Tx phase difference ϕ between both two elements of

$$\phi_\alpha = -\frac{2\pi}{\lambda_0}\Delta x \sin\left(-\alpha_{\mathrm{steer}}\right) \text{ and} \tag{10}$$

$$\phi_\varepsilon = -\frac{2\pi}{\lambda_0}\Delta z \sin\left(-\varepsilon_{\mathrm{steer}}\right), \tag{11}$$

is determined from the group factor [32]

$$\mathrm{GF}(\varphi) = 2\cos\left(0.5\left(\frac{2\pi}{\lambda_0} d \sin\left(-\varphi\right) + \phi\right)\right), \tag{12}$$

with the element spacing d and the incidence angle φ. Due to the factor of 2 in the GF, a directional gain of 3 dB arises in the main beam direction. Additionally, the Tx power is doubled as it is generated in two individual channels. Thus, a gain of 6 dB results for both beamforming modes. In the elevation direction, the steering range is limited to ±12.8°, due to the large element spacing. Nevertheless, this still covers the 3 dB beamwidth and thus the FoV in this operating mode, cf. Table 2. No grating lobes occur, since the Tx antenna group is fully populated with radiating elements.

III. SYSTEM REALIZATION

The realized 1728 channel 4D imaging radar demonstrator is shown in Fig. 5(a). The back side of the PCB, as shown in (b), holds the 12 radar MMICs, their related SMD parts, the power supply and the reference clock distribution. The length of the RO lines in the feedthrough topology is chosen to result in a shift of 4 δR. Therefore, the shifts can easily be corrected, and a circulating linear frequency modulation MIMO operation [33] is possible as well. As specified in Section II.B, only the antennas are placed on the front side of the PCB, see (c). The remaining space is filled with a low radar cross section (RCS) structure as introduced in [34] to balance the copper allocation on the top and bottom layer and thus to ensure manufacturability.

In Fig. 6(a), a close up of a single antenna is shown. Each antenna consists of four patches in the elevation direction to illuminate the scenario with an antenna gain of 12.4 dBi. The 10 dB beamwidth is 130° in the azimuth and 36° in the elevation plane, respectively, as shown by the antenna pattern in Fig. 6(b). In the azimuth direction, parasitic patches are used to enhance the bandwidth to fully cover the 76 GHz to 81 GHz operating range. The four main patches are fed individually with an H-shaped coupling aperture in L02 between patch and serial feed in layer L03 (see Fig. 2). The patch distance of 2.15 mm is optimized for radiation into broadside direction.

A Xilinx Zynq MPSoC is used to control the system and to collect the 48 receive data streams with a total data rate of 28.8 Gbit/s. Via an integrated router, the radar sensor is

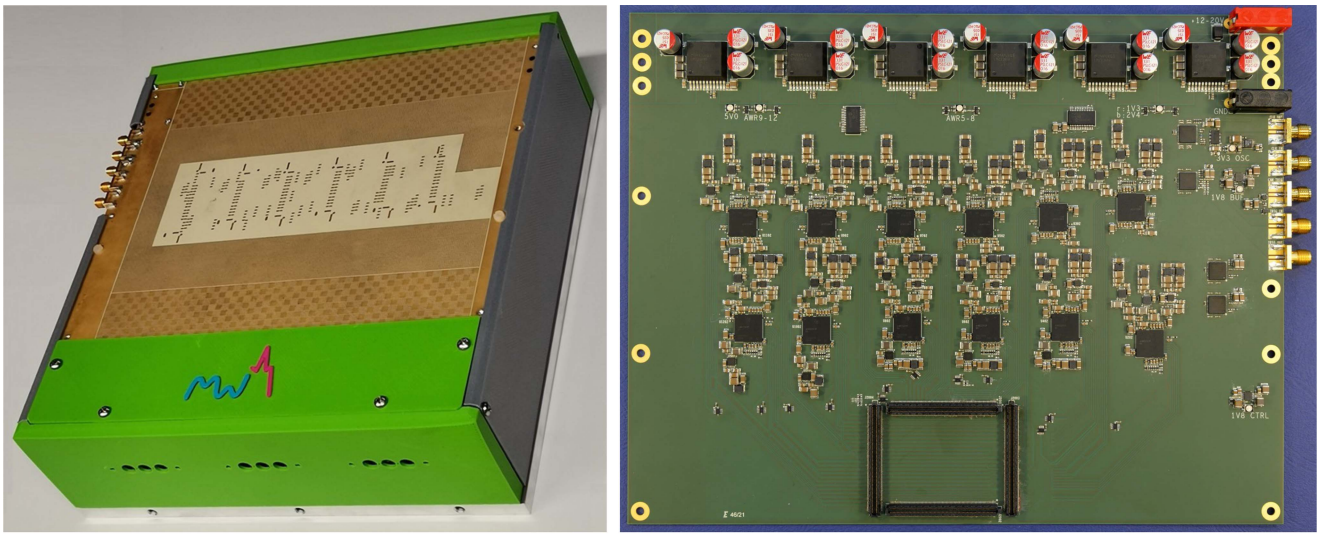

(a) (b)

(c)

FIGURE 5. Realized 4D imaging radar: (a) photograph of the demonstrator with a size of 262 mm × 272 mm × 85 mm, (b) back side of the assembled PCB with a size of 250 mm × 195 mm, and (c) antenna frontend on the front side of the PCB with a hardware aperture of 184 mm × 40.5 mm.

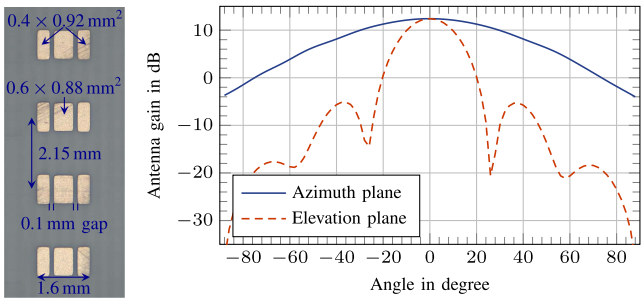

(a) (b)

FIGURE 6. Realized antenna element with feed in layer L03, an H-shaped coupling aperture in layer L02 and 1 × 4 microstrip patch antennas with parasitic elements on the top layer: (a) photograph and (b) antenna gain.

TABLE 3. Overview of the Radar Parameters Used in This Paper

Ramp duration T	34.4 µs
Ramp repetition time T_r	42 µs
Ramp start frequency f_0	76 GHz
RF bandwidth B	5 GHz
Number of samples N_s	1536
Number of chirps N_c	1152
Number of virtual channels N_{Vx}	1728 = 36 Tx × 48 Rx
Virtual aperture A_V	85.2 λ_0 (az.) × 14.8 λ_0 (el.)
Multiplexing scheme	TDM
Receiver gain	48 dB

controlled with either a WiFi, LAN, or WAN connection. All building blocks of the radar are supplied with the same 12-to-20 V line, enabling independent measurements with a battery pack or on a vehicle. The radar parameters as used in the measurements in this paper are summarized in Table 3.

With this setting, a maximum range of 23 m and a range resolution of 3 cm is achieved, as the radar MMIC's full bandwidth of 5 GHz is utilized. The radar parameters may be changed according to [27].

The raw time data of all Rx channels is processed using conventional range-Doppler processing [28]. Afterwards, the range shift due to the feedthrough topology is corrected (see Section II.A), the steering vectors of the range-Doppler cells

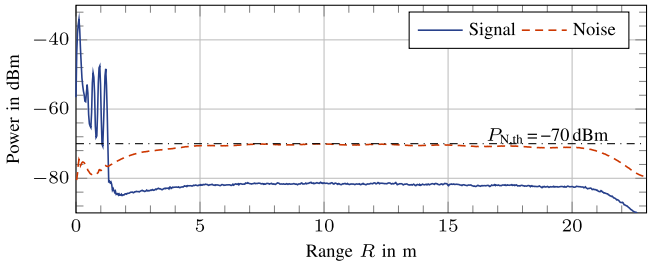

FIGURE 7. Radar measurement into free space. The four peaks between 0.3 m and 1.2 m occur due to the applied range correction.

of interest are extracted [35], and 2D DoA estimations [6] are performed to obtain the 4D information of the scene.

IV. VERIFICATION BY RADAR MEASUREMENTS

The performance of the radar sensor is validated by measurements of known objects. To determine the noise power, the standard deviation over all measured ramps is calculated [36]. In the range spectra, the non-coherent integration of the results of the 1728 2D Fourier transforms (FTs) is shown as it is used for the target extraction [35].

A. DETECTION PERFORMANCE

The detection performance is verified with a measurement into free space as shown in Fig. 7. The thermal noise power $P_{N,th}$ [37] of the utilized FMCW radar system is

$$P_{N,th} = \frac{k_B \cdot T_0}{T} = \frac{k_B \cdot 290\,\mathrm{K}}{34.4\,\mu\mathrm{s}} = -129\,\mathrm{dBm}\,, \tag{13}$$

with the Boltzmann constant k_B, the standard noise temperature T_0, and the ramp duration T. For the Rx gain of 48 dB, the noise figure of the radar transceiver is 11 dB [27]. Eventually, the noise power is −70 dBm in the intermediate frequency (IF) spectrum, which is in perfect agreement with the measurement shown in Fig. 7. As can be seen, the noise power is reduced for small and large ranges. This is due to the influence of the IF high-pass filter to suppress strong Tx-Rx leakage and the anti-aliasing low-pass filter.

For ranges greater than 1.5 m, the range spectrum is completely free of spurious detections. The four peaks visible after the Tx-Rx leakage occur due to the feedthrough topology and the index correction of (4). With the main leakage peak visible at the 4th range cell and $\Delta i_{R,\,FTT} = 4$, according to (3) the worst case is a shift to $i_{R,\,Rx} = -16$. Due to the real sampling and the correction by +20 range cells, the farthest Tx-Rx leakage peak is predicted to be visible at $i_{R,\,corr}$=36, corresponding to a range of 1.08 m. However, in the measurement shown in Fig. 7, the last Tx-Rx leakage peak is visible at 1.2 m. This mismatch is caused by additional time delays within the MMICs. Thus, the actually measured $\Delta i_{R,\,FTT}$ equals 4.5. If the correction is performed without zeropadding, a negligible power loss occurs due to the necessary rounding [26].

To further verify the performance, a measurement setup as shown in Fig. 8(a) is employed: A sphere with a diameter of 24.8 cm and RCS of $\sigma = -13$ dBsm is measured in an anechoic chamber at a distance of 4.89 m to the radar. The corresponding range spectrum and range-Doppler image are depicted in (b) and (c), respectively. The sphere is detected with an SNR of 33 dB with respect to the noise floor of the 2D FT at −80 dBm. Between ranges of 2 m to 5.5 m, the sidewalls of the chamber are detected with an SNR of up to 20 dB, and the back wall at around 6 m is visible with up to 27 dB SNR. The rest of the range-Doppler spectrum is free from any spurious or ghost targets.

The received power P_{Rx} can be estimated using the radar equation [38]

$$P_{Rx} = P_{Tx} G_{Tx} G_{Rx} \frac{\lambda_0^2}{(4\pi)^3} \frac{1}{R^4} \sigma\,, \tag{14}$$

with the transmit power P_{Tx} and the transmit and receive gain G_{Tx} and G_{Rx}, respectively. For the sphere, this results in a received power of −44.8 dBm, with $P_{Tx} = 13$ dBm [27], antenna gains of 12.4 dBi each, and a receiver gain of 48 dB. Additionally, 2 dB losses of each vertical transition and 2.5 dB average loss in each antenna feed line are considered. This is in good agreement with the measured value of −46.8 dBm, as observable in Fig. 8(b).

B. DOA ESTIMATION PERFORMANCE

In the 2D DoA estimation shown in Fig. 8(d), six sidelobes are visible with a slightly higher SLL as for the simulated array shown Fig. 4(e). Considering the 2D DoA estimation result shown in Fig. 8(e) for the detachable back wall element (□) shows that both shape and size of this extended target can be estimated well due to the low SLL. Moreover, with a measured angular size of about 10° in both azimuth and elevation and a distance of 5.9 m, the estimated size agrees well with its actual size of 1 m by 1 m.

Finally, the high resolution imaging capability of the system is verified with the range-azimuth cut of the measured scene shown in Fig. 8(f). As the measured power level of the sphere greatly exceeds the axis scaling in (f), the sidelobes with an SLL of 30 dB are visible. Both width (4 m) and length (6.2 m) of the chamber are clearly recognizable. Moreover, with the high separation capabilities in range and angle, even all 28 rows of larger absorber tips on the sidewalls can be distinguished. Also, the detachable back wall can be recognized and distinguished back wall.

C. ANGULAR SEPARABILITY

In Fig. 9(a) and (d), the angular spectra for a corner reflector with an RCS of −5 dBsm measured at a distance of 5 m are shown. These measurements verify the theoretical beamwidths of 0.78° and 3.6° in the azimuth and elevation plane, respectively. To show the angular separation capability, measurements of two close targets separated only by about the beamwidths in azimuth or elevation are depicted in Fig. 9(b)

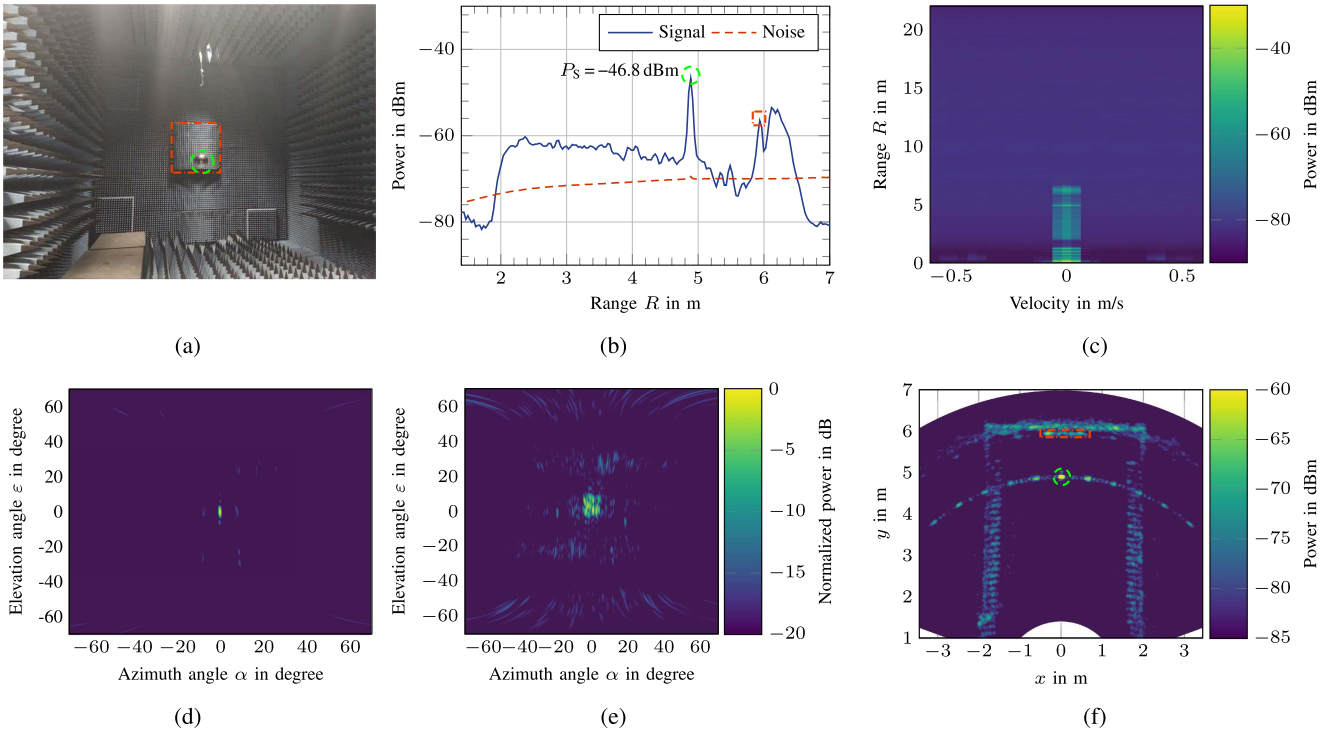

FIGURE 8. Radar measurements of a sphere (○) with a diameter of 24.8 cm at a distance of 4.89 m in front of a detachable back wall element (▭) in an anechoic chamber: (a) photograph of the scenario, (b) range spectrum, (c) range-Doppler plot, (d) 2D angle estimation for the sphere at broadside direction, (e) 2D angle estimation for the detachable back wall element, and (f) azimuth cut of the processed 4D radar image.

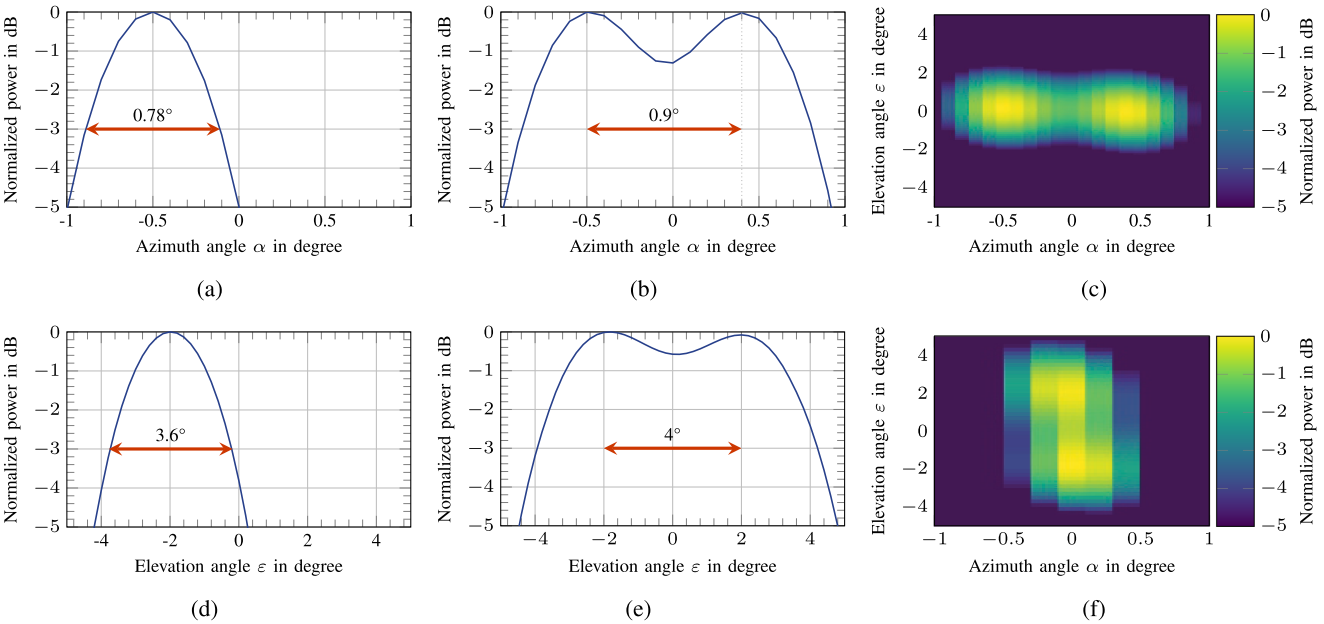

FIGURE 9. Measured angular spectra for one or two targets in the same range-Doppler cell to verify the angular separability in the azimuth plane ((a)–(c)) and in the elevation plane ((d)–(f)): (a) and (d) show the beamwidth for the estimation of a single target, (b) and (e) the angular separability of two targets, and (c) and (f) the corresponding 2D angle estimations.

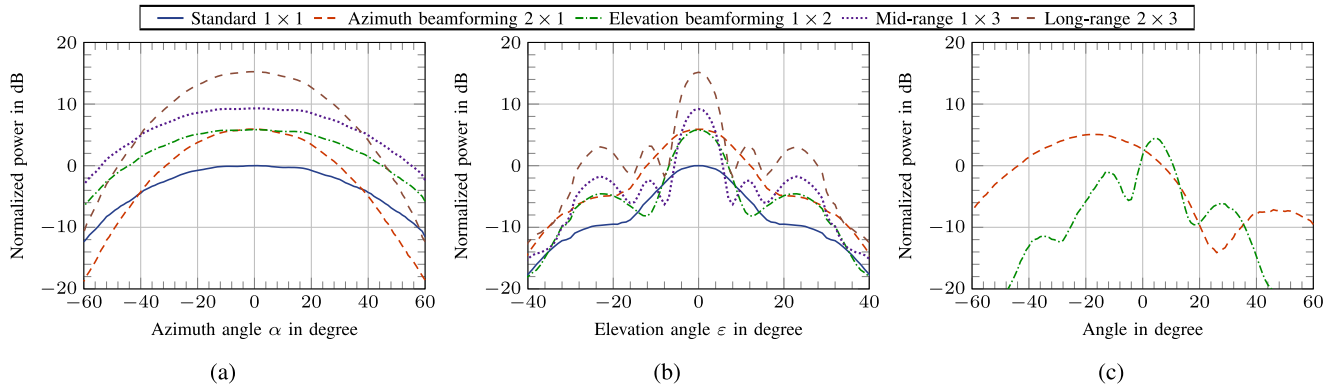

FIGURE 10. Measured two-way radiation pattern normalized to the maximum gain of the standard mode (—): (a) in the azimuth, (b) the elevation plane, and (c) with the beam steered in azimuth towards −30° (- -) and in elevation towards 7.5° (-·-).

and (e), respectively. The results show that the two corner reflectors can be separated in the same range-Doppler cell with a minimum notch in the angular spectrum. The corresponding DoA estimation results are depicted in (c) and (f), respectively.

D. TX BEAMFORMING CAPABILITY

The basic Tx beamforming capability is first verified with beams in broadside direction. Measurements are performed with the measurement setup of Fig. 8(a) after a Tx phase calibration to correct the Tx phase differences ϕ to zero. The sphere is measured over a wide angular range, and the received power is averaged over all virtual channels to obtain the two-way antenna patterns as shown in Fig. 10(a) and (b) for the azimuth and elevation plane, respectively. The expected gain of 6 dB compared to the standard mode is achieved for both the azimuth (- -) and elevation (-·-) beamforming mode in both planes. Furthermore, this gain applies for the entire azimuth plane in the elevation beamforming mode and for the entire elevation plane in the azimuth beamforming mode, since in both cases the number of patches in the respective plane is the same as that of the standard case. Likewise, the beamwidth is reduced in the azimuth plane for the azimuth beamforming mode, while it is reduced in the elevation plane for the elevation beamforming mode. In all modes, the achieved gain depends on the total number of antenna elements, as listed in Table 2. The measured respective gains for the mid- and long-range mode are 9.3 dB and 15.3 dB, which differs only by 0.7 dB from the expected ones. For an identical number of antenna elements in the corresponding plane, the curve progressions and beamwidths are the same, with the narrowest beam but highest gain in the long-range case.

Additionally, the beamforming capability is verified with two steered beams: towards $\alpha_{\text{steer}} = -30°$ with $\phi_\alpha = \pi/2$ in the azimuth beamforming case and $\varepsilon_{\text{steer}} = 7.5°$ with $\phi_\varepsilon = -0.59\pi$ in the elevation beamforming case. The measured beams are shown in Fig. 10(c), where the directional gain applies to the two-way pattern of the non-beamforming case, e.g. at an angle of −30° in azimuth: −2.2 dB (— in (a)) + 6 dB = 3.8 dB (- - in (c)). Thus, the measured maximum is visible at −17.5° with a magnitude of 5.1 dB. The same applies to the elevation beamforming case, with the maximum visible at 4.5° with a magnitude of 4.5 dB. This shift between theoretical and measured steering angle must be considered when steering the beams, as it reduces the steering range.

V. MEASUREMENT OF AN AUTOMOTIVE SCENARIO

Finally, radar measurements are conducted in a parking lot, representing a typical automotive scenario. The observed stationary scenario is depicted in Fig. 11(a). Stationary scenarios are more challenging for radars, representing a corner case for the high resolution imaging radar.

Investigating the measurement results shown in Fig. 11(b) and (c) validates that even typically weak radar targets like a pedestrian or a wooden fence at the edge of the FoV can be identified in the side view of the range-Doppler plot (b). The azimuth cut as shown in (c) gives a detailed image of the evaluated scene. For the three cars closest to the sensor, the characteristic L-shape of cars is visible. Both length and width of the cars can be estimated. Since the nearest car is visible at a large azimuth angle, less scattering centers are detected at the front of the car, due to the attenuation at the edges of the two-way antenna pattern. However, due to the large number of scattering centers detected at the rear of the car, its width can be estimated with high precision. The most distant car is obscured by a closer one, so that only the rear of this vehicle can be detected.

Due to the vertically polarized antennas, the vertical posts of the fence are detected with a larger SNR compared to the horizontal rail. Thus, the fence can be identified as individual scatterers on a straight line in the range-azimuth cut. Both the pedestrian and the street lamp are visible as point targets with large SNR. Despite the sidelobes, the sensor is capable of generating detailed, high-resolution images from single snapshots of the observed scene without the need for multiple measurements and complex post-processing as for synthetic aperture radar or grid maps as shown in [39].

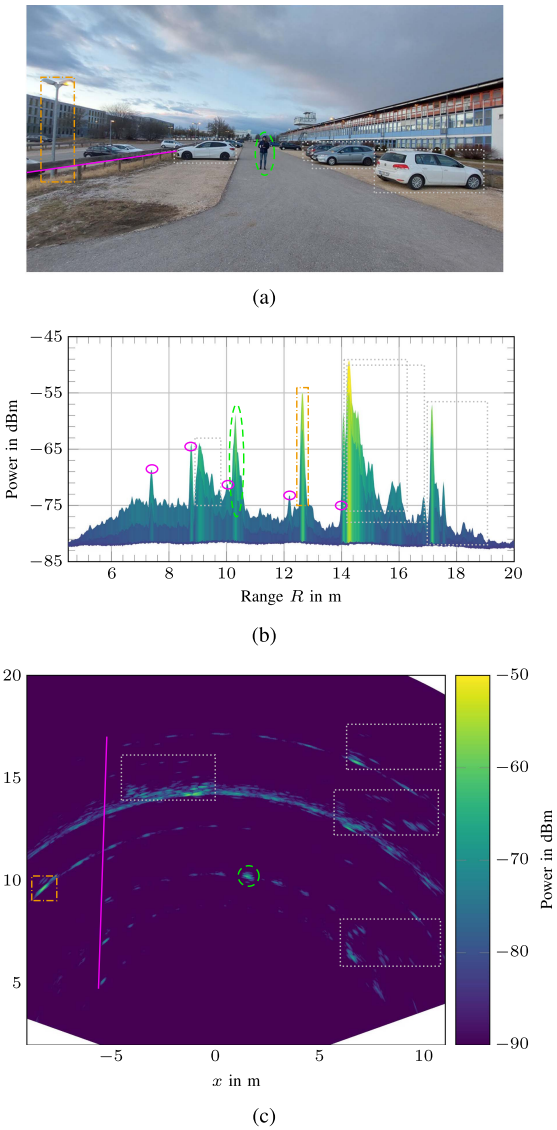

FIGURE 11. **Measurement of a parking lot as an automotive scenario: (a) photograph, (b) side view on the range-Doppler plot, and (c) azimuth cut of the processed 4D radar image. Parked cars are highlighted as (▭), the pedestrian as (○), the street light as (▭), and the fence as (—).**

VI. CONCLUSION

In this paper, a novel high-resolution 4D imaging radar design is presented. Based on a mixed feedthrough and distribution network topology, a system with 12 MMICs is realized. In this way, a system is realized with 36 Tx and 48 Rx channels, resulting in 1728 virtual channels, which exceeds the state-of-the-art channel count by a factor of 9. It is shown that with the use of the 2D maximal SLL matrix, the 4D ambiguity function and thus the ambiguity-free region and the SLL of 2D antenna arrays can be easily assessed, which simplifies the array design.

A novel PCB concept is presented with all components assembled on the back side, the RF signal distribution in a buried layer and only antennas on the front side to minimize parasitic radiation from MMICs or RF transmission lines and to allow for an arbitrary placement of the antennas close to the MMICs. The MIMO antenna array is designed to enable Tx beamforming and to keep the RF transmission line lengths short by realizing a sparse array with interleaved Tx and Rx channels.

The radar's virtual aperture covers 85.2 λ_0 in the azimuth and 14.8 λ_0 in the elevation plane and has an ambiguity-free region of 130° × 75° with a maximal SLL of −15 dB. Two targets with an angular distance of 0.9° or 4° in azimuth or elevation, respectively, can be separated due to the sensor's 3 dB beamwidth of 0.78° × 3.6°. With a fill factor of 38 % of the sparse array, DoA estimations can be performed robustly even at bad conditions as low SNR or multiple scattering centers of an extended target. The outstanding sensitivity and resolution in range and angle is exemplarily demonstrated by showing that the individual absorber tips of an anechoic chamber can be detected and separated in a range-azimuth cut. Detailed high-resolution images can be obtained from single shot radar measurements as it is shown for the automotive parking lot scenario. The obtainable radar images of the proposed system have a high level of detail and quality comparable to grid maps or synthetic aperture radar images and thus provide an unprecedented density of information with only a single measurement.

REFERENCES

[1] P. Hügler, F. Roos, M. Schartel, M. Geiger, and C. Waldschmidt, "Radar taking off: New capabilities for UAVs," *IEEE Microw. Mag.*, vol. 19, no. 7, pp. 43–53, Nov./Dec. 2018.

[2] M. Zink et al., "TanDEM-X: The new global DEM takes shape," *IEEE Geosci. Remote Sens. Mag.*, vol. 2, no. 2, pp. 8–23, Jun. 2014.

[3] S. S. Ahmed, A. Genghammer, A. Schiessl, and L.-P. Schmidt, "Fully electronic E-band personnel imager of 2 m^2 aperture based on a multistatic architecture," *IEEE Trans. Microw. Theory Techn.*, vol. 61, no. 1, pp. 651–657, Jan. 2013.

[4] J. Hasch et al., "Millimeter-wave technology for automotive radar sensors in the 77 GHz frequency band," *IEEE Trans. Microw. Theory Techn.*, vol. 60, no. 3, pp. 845–860, Mar. 2012.

[5] W. Menzel, "Millimeter-wave radar for civil applications," in *Proc. 7th Eur. Radar Conf.*, 2010, pp. 89–92.

[6] A. Di Serio, P. Hügler, F. Roos, and C. Waldschmidt, "2D-MIMO radar: A method for array performance assessment and design of a planar antenna array," *IEEE Trans. Antennas Propag.*, vol. 68, no. 6, pp. 4604–4616, Jun. 2020.

[7] J. Wittemeier, A. M. Ahmed, T. N. Tran, A. Sezgin, and N. Pohl, "3D localization using a scalable FMCW MIMO radar design," in *Proc. German Microw. Conf.*, 2020, pp. 100–103.

[8] S. Sun and Y. D. Zhang, "Four-dimensional high-resolution automotive radar imaging exploiting joint sparse-frequency and sparse-array design," in *Proc. IEEE Int. Conf. Acoust., Speech Signal Process.*, 2021, pp. 8413–8417.

[9] Y. Cheng, J. Su, H. Chen, and Y. Liu, "A new automotive radar 4D point clouds detector by using deep learning," in *Proc. IEEE Int. Conf. Acoust., Speech Signal Process.*, 2021, pp. 8398–8402.

[10] J. Bai and L. Zheng, "Radar transformer: An object classification network based on 4D MMW imaging radar," *Sensors*, vol. 21, no. 11, Jun. 2021, Art. no. 3854.

[11] J. Hasch, "Driving towards 2020: Automotive radar technology trends," in *Proc. IEEE MTT-S Int. Conf. Microw. Intell. Mobility*, 2015, pp. 1–4.

[12] C. Waldschmidt, J. Hasch, and W. Menzel, "Automotive radar – from first efforts to future systems," *IEEE J. Microwaves*, vol. 1, no. 1, pp. 135–148, Jan. 2021.

[13] S. M. Patole, M. Torlak, D. Wang, and M. Ali, "Automotive radars: A review of signal processing techniques," *IEEE Signal Process. Mag.*, vol. 34, no. 2, pp. 22–35, Mar. 2017.

[14] L. Maurer, G. Haider, and H. Knapp, "77 GHz SiGe based bipolar transceivers for automotive radar applications – An industrial perspective," in *Proc. IEEE 9th Int. New Circuits Syst. Conf.*, 2011, pp. 257–260.
[15] A. Och, C. Pfeffer, J. Schrattenecker, S. Schuster, and R. Weigel, "A scalable 77 GHz massive MIMO FMCW radar by cascading fully-integrated transceivers," in *Proc. Asia-Pacific Microw. Conf.*, 2018, pp. 1235–1237.
[16] I. Bilik et al., "Automotive multi-mode cascaded radar data processing embedded system," in *Proc. IEEE Radar Conf.*, 2018, pp. 0372–0376.
[17] B. P. Ginsburg et al., "A multimode 76-to-81 GHz automotive radar transceiver with autonomous monitoring," in *IEEE Int. Solid-State Circuits Conf. Dig. Tech. Papers*, 2018, pp. 158–159.
[18] Texas Instruments Incorporated, "SWRU553 A: AWRx cascaded radar RF evaluation module (MMWCAS-RF-EVM)," Feb. 2020. Accessed: May 04, 2021. [Online]. Available: https://www.ti.com/lit/ug/swru553a/swru553a.pdf
[19] J. Kim et al., "79-GHz four-RFIC cascading radar system for autonomous driving," in *Proc. IEEE Int. Symp. Circuits Syst.*, 2020, pp. 1–5.
[20] F. Engels et al., "Automotive radar signal processing: Research directions and practical challenges," *IEEE J. Sel. Topics Signal Process.*, vol. 15, no. 4, pp. 865–878, Jun. 2021.
[21] F. G. Jansen et al., "Simultaneous multi-mode automotive imaging radar using cascaded transceivers," in *Proc. 18th Eur. Radar Conf.*, 2022, pp. 441–444.
[22] M. Stolz, M. Wolf, F. Meinl, M. Kunert, and W. Menzel, "A new antenna array and signal processing concept for an automotive 4D radar," in *Proc. 15th Eur. Radar Conf.*, 2018, pp. 63–66.
[23] D. Zankl et al., "BLASTDAR–A large radar sensor array system for blast furnace burden surface imaging," *IEEE Sensors J.*, vol. 15, no. 10, pp. 5893–5909, Oct. 2015.
[24] M. Kucharski, A. Ergintav, W. A. Ahmad, M. Krstić, H. J. Ng, and D. Kissinger, "A scalable 79-GHz radar platform based on single-channel transceivers," *IEEE Trans. Microw. Theory Techn.*, vol. 67, no. 9, pp. 3882–3896, Sep. 2019.
[25] R. Zhou et al., "A two-chip cascaded FMCW radar for 2D angle estimation," in *Proc. IEEE MTT-S Int. Wireless Symp.*, 2021, pp. 1–3.
[26] D. Schwarz et al., "System performance of a scalable 79 GHz imaging MIMO radar with injection-locked LO feedthrough," *IEEE J. Microwaves*, vol. 1, no. 4, pp. 941–949, Oct. 2021.
[27] Texas Instruments Incorporated, "SWRS223B: AWR2243 single-chip 76- to 81-GHz FMCW transceiver, datasheet," Dec. 2021. Accessed: Apr. 26, 2022. [Online]. Available: https://www.ti.com/lit/ds/symlink/awr2243.pdf
[28] V. Winkler, "Range doppler detection for automotive FMCW radars," in *Proc. 4th Eur. Radar Conf.*, 2007, pp. 1445–1448.
[29] A. Dürr, R. Kramer, D. Schwarz, M. Geiger, and C. Waldschmidt, "Calibration-based phase coherence of incoherent and quasi-coherent 160-GHz MIMO radars," *IEEE Trans. Microw. Theory Techn.*, vol. 68, no. 7, pp. 2768–2778, Jul. 2020.
[30] D. Schwarz, N. Riese, A. Dürr, and C. Waldschmidt, "A broadband multilayer vertical transition at 79 GHz employing FR4 as core material," in *Proc. 51st Eur. Microw. Conf.*, 2022, pp. 700–703.
[31] M. Eric, A. Zejak, and M. Obradovic, "Ambiguity characterization of arbitrary antenna array: Type I. Ambiguity," in *Proc. IEEE 5th Int. Symp. Spread Spectr. Techn. Appl. - Proc. Spread Technol. Afr. (Cat. No.98TH8333)*, 1998, vol. 2, pp. 399–403.
[32] C. A. Balanis, *Antenna Theory: Analysis and Design*, 2nd ed. Hoboken, NJ, USA: Wiley, 1997.
[33] H. Sun, F. Brigui, and M. Lesturgie, "Analysis and comparison of MIMO radar waveforms," in *Proc. Int. Radar Conf.*, 2014, pp. 1–6.
[34] C. Vasanelli, F. Bögelsack, and C. Waldschmidt, "Reducing the radar cross section of microstrip arrays using AMC structures for the vehicle integration of automotive radars," *IEEE Trans. Antennas Propag.*, vol. 66, no. 3, pp. 1456–1464, Mar. 2018.
[35] C. Vasanelli et al., "Calibration and direction-of-arrival estimation of millimeter-wave radars: A. practical introduction," *IEEE Antennas Propag. Mag.*, vol. 62, no. 6, pp. 34–45, Dec. 2020.
[36] A. Dürr et al., "High-resolution 160-GHz imaging MIMO radar using MMICs with on-chip frequency synthesizers," *IEEE Trans. Microw. Theory Techn.*, vol. 67, no. 9, pp. 3897–3907, Sep. 2019.
[37] K. Thurn, R. Ebelt, and M. Vossiek, "Noise in homodyne FMCW radar systems and its effects on ranging precision," in *IEEE MTT-S Int. Microw. Symp. Dig.*, 2013, pp. 1–3.
[38] M. I. Skolnik, *Introduction to Radar Systems*, 2nd ed. New York, NY, USA: McGraw-Hill, 1980.
[39] T. Grebner, P. Schoeder, V. Janoudi, and C. Waldschmidt, "Radar-based mapping of the environment: Occupancy grid-map versus SAR," *IEEE Microw. Wireless Compon. Lett.*, vol. 32, no. 3, pp. 253–256, Mar. 2022.

DOMINIK SCHWARZ (Graduate Student Member, IEEE) received the M.Sc. degree, from Ulm University, Ulm, Germany, in 2018, where he is currently working towards the Ph.D. degree. From 2011 to 2018, he was a student trainee with Hensoldt Sensors, Ulm, Germany. In 2018, he joined the Institute of Microwave Engineering, Ulm University. His current research interest includes automotive MIMO radars with a focus on high bandwidths, high channel counts, 2D-DoA estimation, and novel multilayer PCB structures at millimeter-wave frequencies. Mr. Schwarz was a recipient of the Ingenieure für Kommunikation Award in 2016 and the Argus Science Award in 2019.

NICO RIESE received the M.Sc. degree, in electrical engineering from Ulm University, Ulm, Germany, in 2022, where he is currently working towards the Ph.D. degree with the Institute of Microwave Engineering, Ulm, Germany. His current research interests include novel waveguide and passive transition structures as well as antenna concepts applicable for multi-frequency radar systems in the micro- and millimeter-wave range.

INES DORSCH (Graduate Student Member, IEEE) received the M.Sc. degree, in electrical engineering from Ulm University, Ulm, Germany, in 2019, where she is currently working towards the Ph.D. degree with the Institute of Microwave Engineering, Ulm, Germany. Her current research interests include biomimetic antenna systems in the microwave and millimeter-wave range and their applications in sensor networks. Ms. Dorsch was the recipient of the Piergiorgio L. E. Uslenghi Letters Prize Paper Award in 2022 and the ARGUS Science Award in 2019.

CHRISTIAN WALDSCHMIDT (Fellow, IEEE) received the Dipl.-Ing. (M.S.E.E.) and the Dr.-Ing. (Ph.D.E.E.) degrees from the University Karlsruhe, Karlsruhe, Germany, in 2001 and 2004, respectively. From 2001 to 2004, he was a Research Assistant with the Institut für Höchstfrequenztechnik und Elektronik, Universität Karlsruhe, Germany. Since 2004, he has been with Corporate Research and Chassis Systems, Robert Bosch GmbH. He was heading different research and development teams in microwave engineering, RF-sensing, and automotive radar. In 2013, he returned to academia and was appointed as the Director of the Institute of Microwave Engineering with Ulm University, Ulm, Germany, as Full Professor. He authored or coauthored more than 200 scientific publications and more than 20 patents. His research interests include focus on radar and RF-sensing, mm-wave and submillimeter-wave engineering, antennas and antenna arrays, and RF and array signal processing. Prof. Waldschmidt is a Member of the Executive Committee Board of the German MTT/AP Joint Chapter and a Member of the German Information Technology Society (ITG). He was the Chair of the IEEE MTT-27 Technical Committee on wireless enabled automotive and vehicular applications. He was the two-time TPC Chair and the General Chair of the IEEE MTT International Conference on Microwaves for Intelligent Mobility. Since 2018, he has been an Associate Editor for IEEE MICROWAVE WIRELESS COMPONENTS LETTERS. He is a reviewer for multiple IEEE transactions and many IEEE conferences in the field of microwaves. He has been the co-recipient of 12 best paper awards since 2014.